Huang *et al. Biochar* (2025) 7:29
https://doi.org/10.1007/s42773-024-00419-x

Biochar

ORIGINAL RESEARCH Open Access

# Efficient recovery of rare metal lanthanum from water by MOF-modified biochar: DFT calculation and dynamic adsorption

Qilan Huang[1], Qianru Zhang[1*], Shuwen Zhao[1], Chuchen Zhang[1], Huixin Guan[2] and Jianqiao Liu[2*]

## Abstract

In this research, a novel metal-organic framework-modified biochar composite (MIL-88b@BC) was created for the first time by modifying rice husk biochar using the excellent adsorption properties of metal-organic framework (MOF), as well as reducing the solubility of MOF using biochar as a substrate, aiming to improve the understanding of the adsorption characteristics of rare-earth metal recycling and to predict its adsorption mechanism. Density functional theory (DFT) computations allowed for rationally constructing the adsorption model. According to DFT calculations, the primary processes involved in the adsorption of $La^{3+}$ were $\pi$–$\pi$ interaction and ligand exchange, wherein the surface hydroxyl group played a crucial role. MIL-88b@BC interacted better with $La^{3+}$ than biochar or MOF did. Accompanying batch tests with the theoretical conjecture's verification demonstrated that the pseudo-second-order model and the Langmuir model, respectively, provided a good fit for the adsorption kinetics and isotherms. The maximum $La^{3+}$ adsorption capacity of MOF@BC (288.89 mg $g^{-1}$) was achieved at pH 6.0, which was significantly higher than the adsorbents' previously documented adsorption capacities. Confirming the DFT estimations, the adsorption capacity of BC@MIL-88b for $La^{3+}$ was higher than that of MOF and BC. Additionally, MOF@BC can be recycled at least four times. To mitigate the growing scarcity of rare earth elements (REEs) and lessen their negative environmental effects, this work laid the path for effectively treating substantial volumes of wastewater produced while mining REEs.

## Highlights

- The novel composite adsorbent was prepared by MOF and biochar in situ growth method.
- The adsorption mechanism was innovatively investigated based on DFT calculations.
- Ligand exchange and La–O–Fe formation dominated in lanthanide ion removal.

**Keywords** Biochar, Fe-MOF, Adsorption, Rare earth element, Density functional theory

*Correspondence:
Qianru Zhang
zhangqianru@caas.cn
Jianqiao Liu
jqliu@dlmu.edu.cn

**Graphical Abstract**

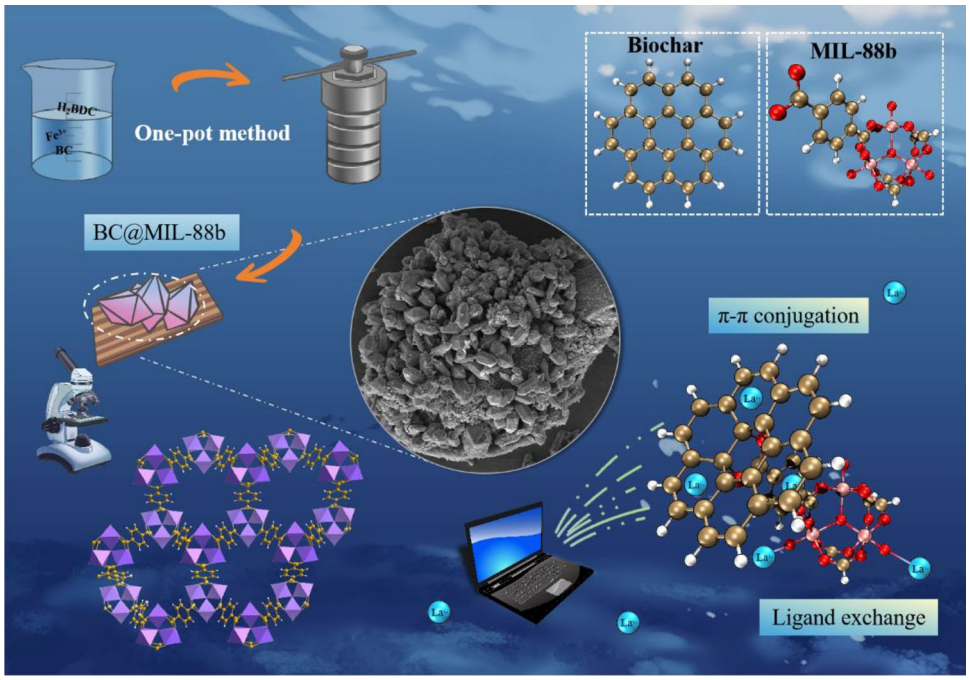


## 1 Introduction

Rare earth elements (REEs) encompass the elements La–Lu, Sc, and Y (Al Momani et al. 2023), which exhibit advantageous physicochemical properties and are often termed "industrial vitamins" because of their strategic importance for countries seeking to develop high-precision industries (Binnemans et al. 2013). REE mining generates large amounts of low-concentration effluent (0.8–130 mg $L^{-1}$) and thus results in REE waste (Migaszewski and Galuszka 2015). Given the scarcity and non-renewability of REE resources and the nonbiodegradability and toxicity of REE ions (Edahbi et al. 2019), REE recycling is of high economic and environmental significance (Kim et al. 2022).

The REE recovery methods developed to date include those based on chemical sedimentation, adsorption, extraction, and ion exchange (Huang et al. 2017; Okamura and Hirayama 2021; Li et al. 2015). Among them, adsorption offers the benefits of eco-friendliness, low cost, selectivity, and effectiveness at low concentrations (Borges et al. 2020). It is a challenging task to design an efficient and economical adsorbent for recycling treatment. Various kinds of adsorbents have been created to extract rare earth ions from aqueous solutions, including clay minerals (Iftekhar et al. 2017a), zeolite imidazolate skeletons (Abdel-Magied et al. 2019), cellulose nanocomposites (Iftekhar et al. 2017b), and graphene oxide-based nanocomposites (Zhao et al. 2021). However, their poor adsorption capacity restricts their use on a broad scale for rare earth ion recovery, emphasizing the need for innovative materials.

The carbon-rich solid known as biochar (BC) is created when biomass is pyrolyzed in anaerobic or anoxic environments. It is a valuable tool for eliminating organic and heavy metal pollutants from the environment. Meanwhile, biochar is environmentally friendly, affordable, and adaptable, converting a wide range of agricultural and human-made wastes, including rice husks, straw, and manure, into wealth. The production of BC also contributes to the mitigation of the greenhouse effect, which is consistent with the dual-carbon strategy. Adsorption effectiveness of BC is mostly determined by its exterior functional groups and high specific surface area (Yan et al. 2024). However, the virgin BC has a low specific surface area, an undeveloped pore structure, few active sites, a limited adsorption capacity, and low selectivity in actual. As a result, it requires modification. Chemical modification (e.g., chemical treatment of acids, bases, metal oxides, and organic compounds before and after biomass feedstock pyrolysis) and physical modification (e.g., steam activation and ball milling) create altered biochar (Zhang et al. 2024a). A vast

number of research have concentrated on modifying BC to increase its efficiency in pollution removal. Han et al. developed $ZnFe_2O_4$ (ZF) modified porous biochar (PBC/ZF), which showed better performance than original biochar in terms of specific surface area and Ce (IV) adsorption capacity in rare earth wastewater (Han et al. 2023). Wang et al. prepared ammonium citrate (AC) modified biochar. The adsorption capacity of AC@BC for La (III) was 2.1 times that of the original biochar prepared at the same temperature (Wang et al. 2016). The above investigations demonstrated that the modified biochar successfully improved adsorption performance. However, the modification technique must be carefully chosen owing to considerations such as secondary pollution, cost, and yield (Du et al. 2023).

Metal-organic framework (MOF) is a novel class of crystalline porous material made up of coordination bonds connecting metal nodes to organic ligands. Compared to conventional adsorbents, it is highly effective at removing pollutants from water due to its rich functional groups, huge specific surface area, porosity, etc. The most important feature of MOF is its structural versatility and designability, which allows the structure to be customized according to a specific application, and the selective binding of desired elements in the presence of different interferences. Compared with divalent metals, such as Zn and Cu, Fe can attain a higher valence state and thus engage in stronger metal–ligand interactions and form MOFs with higher hydrothermal stability (Devic and Serre 2014). The magnetic effect and chemical and hydrolytic stability of iron-based MOFs make them ideally suited for capturing contaminants from water by adsorption. Although the Lewis-acidic REEs often form complexes with oxygenated functional groups and are readily adsorbed onto MOFs, the small particle size and nonnegligible water solubility of MOF powders limit their application scope, particularly in continuous-flow systems. And although Fe-doped biochar composites have been successfully used for the adsorption of metal ions and have shown excellent adsorption properties (Hudcová et al. 2022), Fe-MOF-doped biochar composites or even other metal ion-doped biochar composites are rarely reported, and there is no precedent for the adsorption of rare earth ions.

As a result, magnetic MOF-modified BC composite aims to use BC as a carrier to reduce the solubility of MOF, prevent secondary pollution, and improve the recyclability, while also improving the pore volume and specific surface area of the composites, increasing active sites, and ultimately realizing the composites' high efficiency in pollutant adsorption. There have been few publications on MOF@BC and no investigations on its ability to adsorb rare-earth ions. This paper presents an innovative synthesis of a MOF@BC that was used in conjunction with density-functional theory (DFT) computations to simulate the loading behaviour of the adsorbent on rare-earth ions. The atomic and electronic properties of the adsorbent were examined in order to explore the adsorption mechanism of the rare-earth ions from an atomic level.

Herein, a novel rice husk BC@MOF composite was synthesized using MIL-88b(Fe) as a template and evaluated as an adsorbent for REE recovery from aqueous media. As one of the most abundant and useful lanthanides, La is widely used in many fields, including the production of precision optical glass and ceramics, agriculture, steel processing, and catalysis (Wang et al. 2016). However, due to the genotoxicity of La (III) to human peripheral blood lymphocytes, the wastewater containing La discharged in industrial processes will pollute the environment and endanger human health (Yongxing et al. 2000). Therefore, this study chooses La (III) as the research object. The relative mechanisms of three adsorbents on $La^{3+}$ were investigated by using density flooding theory (DFT) calculations. Thermogravimetric studies, $N_2$ adsorption–desorption, X-ray diffraction (XRD), and scanning electron microscopy (SEM) were used to characterise the adsorbents. In addition, we investigated the impacts of pH and coexisting ions, looked at the adsorbent recyclability, and studied the adsorption isotherms, kinetics, and thermodynamics. Fourier transform infrared spectroscopy (FTIR) and X-ray photoelectron spectroscopy (XPS) were used to conjecture the loading mechanism, and the results agreed with DFT simulations. Finally, the $La^{3+}$ recovery performance of the composite adsorbent was evaluated under real-life conditions. Thus, this study paves the way for the ecofriendly and cost-effective recovery of $La^{3+}$ from aqueous media and helps solve one of the main problems of REE mining.

## 2 Materials and procedures

### 2.1 Chemicals

Table S1 lists the origins and specifications of the reagents.

### 2.2 Preparation of materials

Text S1 describes synthetic approaches.

### 2.3 DFT calculations

The interactions between BC, MIL-88b, BC@MIL-88b, and $La^{3+}$ were rationalized using DFT calculations, which were performed using the Device Studio and BDF software (Liu et al. 1997, 2003; Zhang et al. 2020). The GB3LYP functional was used. Due to its precision

and computational range, the 6–31G (d, p) basis set was selected for C, H, and O, whereas the Lanl2dz pseudopotential basis was chosen for Fe and La.

### 2.4 Batch adsorption experiments

The study employed batch adsorption tests with an adsorbent dose of 0.20 g $L^{-1}$ (BC, MIL-88b, and BC@MIL-88b) to examine the impact of several factors, including temperature, pH, coexisting ions, reaction time, and initial $La^{3+}$ concentration, on the adsorption capacity of $La^{3+}$ in water. Every experiment was conducted thrice, and the matching averages of the data were presented. $La^{3+}$ solutions were prepared using lanthanum nitrate and distilled water. Except for the isotherm studies, every batch experiment was carried out with a $La^{3+}$ concentration of 60 mg $L^{-1}$. A thermostatic shaker was used to agitate the adsorbent and $La^{3+}$ solution at 250 rpm. Using an Arsenazo III-based photometric technique, a UV-Visible spectrophotometer (UV-2550, Shimadzu, Japan) was utilised to measure $La^{3+}$ in filtrates (Text S2). Equations (1) and (2) were used to compute the removal rate (R, %) and adsorption capacity ($q_e$, mg $g^{-1}$):

$$q_e = \frac{(C_0 - C_e)V}{m} \tag{1}$$

$$R = \frac{C_0 - C_e}{C_0} \times 100\% \tag{2}$$

### 2.5 Utilization in real water and material regeneration

Using untreated surface runoff near a rare earth mining location in Ganzhou, Jiangxi Province, the practical applicability of BC@MIL-88b for $La^{3+}$ recovery was investigated. The primary characteristics of real water bodies are listed in Table S2. Samples of untreated surface runoff (30 mL) were mixed with different concentrations of the adsorbent and left to react for 24 h at 298 K. The aforementioned photometric technique was used to filter the supernatant and measure the amount of $La^{3+}$ in the filtrate. A dispersion of BC@MIL-88b in a 5 mg $L^{-1}$ $La^{3+}$ solution was agitated at 298 K for 12 h at 250 rpm in order to assess regenerability. Following centrifugation of the reaction mixture, the quantity of $La^{3+}$ in the supernatant was ascertained as previously mentioned. After being dried, the adsorbent was put in 0.05 M HCl. After centrifuging the mixture, the concentration of $La^{3+}$ in the supernatant was measured according to the previously mentioned procedure. After being cleaned with ultrapure water until the pH of the washings was neutral, the adsorbent was dried and put to use again.

### 2.6 Characterization method

Characterization methods are presented in Text S4.

### 2.7 Column tests

Experiments on $La^{3+}$ removal were conducted in a column that was filled with a combination of BC@MIL-88b and quartz sand. The column length is 0.5 m, the inner diameter is 0.4 mm, the outer diameter is 0.6 mm, and the quartz sand has a mesh size of 80–120 (0.1–0.2 mm). For support, fill the column with 5 cm of quartz sand at both the top and bottom. Ten grammes of the mixture, of which BC@MIL-88b has a mass of 200 mg, were placed in the centre of the column. A peristaltic pump operating in bottom-to-top mode at room temperature continuously injected 5 mg $L^{-1}$ of influent water into the column at a rate of 10 mL $min^{-1}$. Ninety minutes was the associated empty bed contact time (EBCT). To ascertain the removal efficiency, the effluent samples were gathered at a predetermined period and their $La^{3+}$ concentration was examined.

## 3 Results and discussion

### 3.1 Characterization of adsorbents

Figure 1a–c presents the representative SEM images of BC, MIL-88b, and BC@MIL-88b, respectively. BC had an interconnected layered porous structure with a smooth surface and no visible material attachment, while

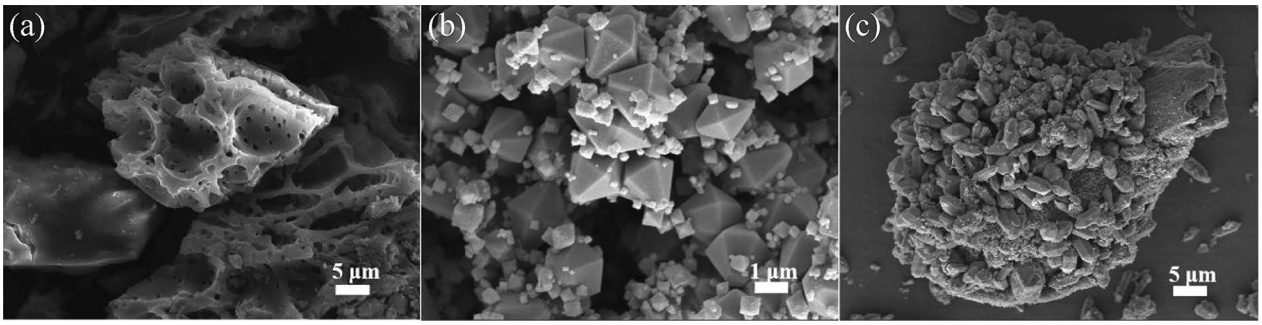


**Fig. 1** SEM images of **a** BC, **b** MIL-88b, and **c** BC@MIL-88b

MIL-88b comprised nanorods with lengths and widths of approximately 1 μm and 200 nm, respectively. BC@MIL-88b retained the lamellar porous structure of BC, although some MIL-88b particles blocked the pores and thus possibly reduced the quantity of active sites.

The XRD patterns of MIL-88b and BC@MIL-88b (but not BC) displayed prominent sharp peaks indicative of high crystallinity (Fig. S1a) (Huang et al. 2022). The effective synthesis of this MOF was validated by the major peaks in the MIL-88b pattern matching those in the related crystal information file (2088535). Similarly, the peaks of BC@MIL-88b closely resembled those of MIL-88b but were shifted to lower diffraction angles (Deng et al. 2023), possibly because of MOF diffusion onto the BC surface or the formation of large interstitials in MOF crystals due to flaws or impurities in BC.

The specific surface areas of the samples BC, MIL-88b, and BC@MIL-88b were 56.27 $m^2\ g^{-1}$, 194.53 $m^2\ g^{-1}$, and 43.23 $m^2\ g^{-1}$, respectively, whereas their pore volumes were 0.017 $cm^3\ g^{-1}$, 0.063 $cm^3\ g^{-1}$, and 0.147 $cm^3\ g^{-1}$. (Table S3). Theoretically, the specific pore volume and specific surface area of BC should rise when MOF particles decorate its surface (Ecer and Yilmaz 2024). Nevertheless, the introduction of MOF particles may also obstruct the internal voids and thus reduce the specific surface area (Wang et al. 2020). BC, MIL-88b, and BC@MIL-88b had average pore sizes of 2.44 nm, 2.23 nm, and 10.05 nm, respectively, and were therefore predominantly mesoporous. The $N_2$ sorption isotherms of all materials (Fig. 2e) were of type IV, as expected for mesoporous adsorbents. The standard isotherm approaches adsorption saturation, with BC, MIL-88b, and BC@MIL-88b curves concluding at the platform's inflection point (Prabhu et al. 2019). Additionally, Fig. S1b shows the narrow hysteresis obtained for MIL-88b@BC. The saturation magnetization strength (Ms) was 0.12 emu $g^{-1}$, which meant that it is intrinsically weakly magnetic. The hysteresis curves obtained indicated that the sample was a magnetic soft material with ferromagnetic properties at room temperature (Qu et al. 2024a).

The thermogravimetric analysis diagram of BC, MIL-88b, and BC@MIL-88b (Fig. 2a) showed that the thermal stability of the composite adsorbent exceeded those of its constituents (Yang et al. 2016). The thermogravimetric analysis diagram of MIL-88b and BC@MIL-88b featured three weight loss stages, whereas two stages were observed for BC. The rapid weight loss between 30 °C and 110 °C (3.8%, 4.6%, and 3.5%, for BC, MIL-88b, and BC@MIL-88b, respectively) was ascribed to the evaporation of water that had been physisorbed on the surface. (Chakhtouna et al. 2021). Between 300 °C and 650 °C was when BC experienced its second weight loss (11.99%), which was caused by the breakdown of lignin and inorganic carbonate (Chakhtouna et al. 2023). The second weight loss of MIL-88b and BC@MIL-88b (27.89%) occurred between 110 °C and 430 °C and reflected the evaporation of solvent molecules trapped within the internal pores. The third weight loss (31.74–34.35%) of MIL-88b and BC@MIL-88b was observed at 430–600 (700) °C and ascribed to ligand carbonization and MOF structure collapse (Jahan et al. 2022). The final product of MOF decomposition was iron oxide (Rad et al. 2021; Zhou et al. 2019). The remarkable structural stability and performance of BC@MIL-88b motivated use to explore its applications.

### 3.2 Computational analysis

Structural optimization and energy calculations were performed for BC, MIL-88b, and BC@MIL-88b to investigate the interaction mechanism. During the

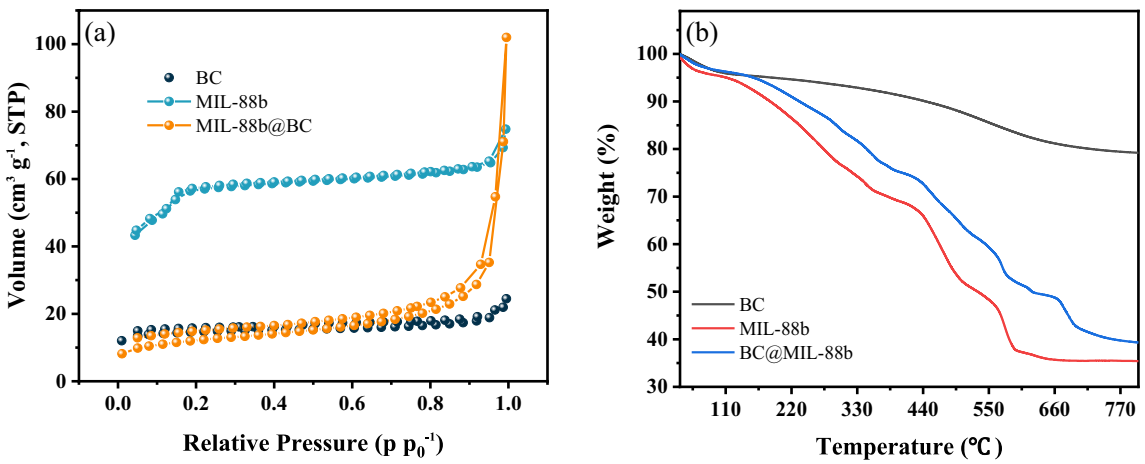


**Fig. 2** **a** $N_2$ adsorption and desorption isotherms, and **b** thermogravimetric curves of BC, MIL-88b, BC@MIL-88b

growth and preparation of BC@MIL-88b, the organic ligands and metal ions in the MOF were selectively bound to the smallest structural units. As the MOF expanded, the smallest structural units established ionic associations with the carbon framework surrounding the oxygenated functional groups of BC. The remaining ligands and metal ions combined near the attachment point to form a BC@MIL-88b secondary structural unit via self-assembly. During this process, some oxygenated functional groups (including carboxyl, carbonyl, and aldehyde groups) of BC prevented MOF expansion. The surface of BC was found to be covered with rod-like MIL-88b structures, as revealed by SEM analysis. We simulated the surface structure of the aromatized biogenic BC using a pure graphene structure to streamline the model calculations. Numerous studies have successfully used this strategy with positive outcomes (Chen et al. 2024; Zhang et al. 2024b). Given the large cell structures of Fe-based MOFs, a cluster model with Fe as the node and a mono-ligand with carboxyl groups on the surface were chosen to improve computational efficiency. The structural models of BC, MIL-88b, and MIL-88b@BC are shown in Fig. 3a–c.

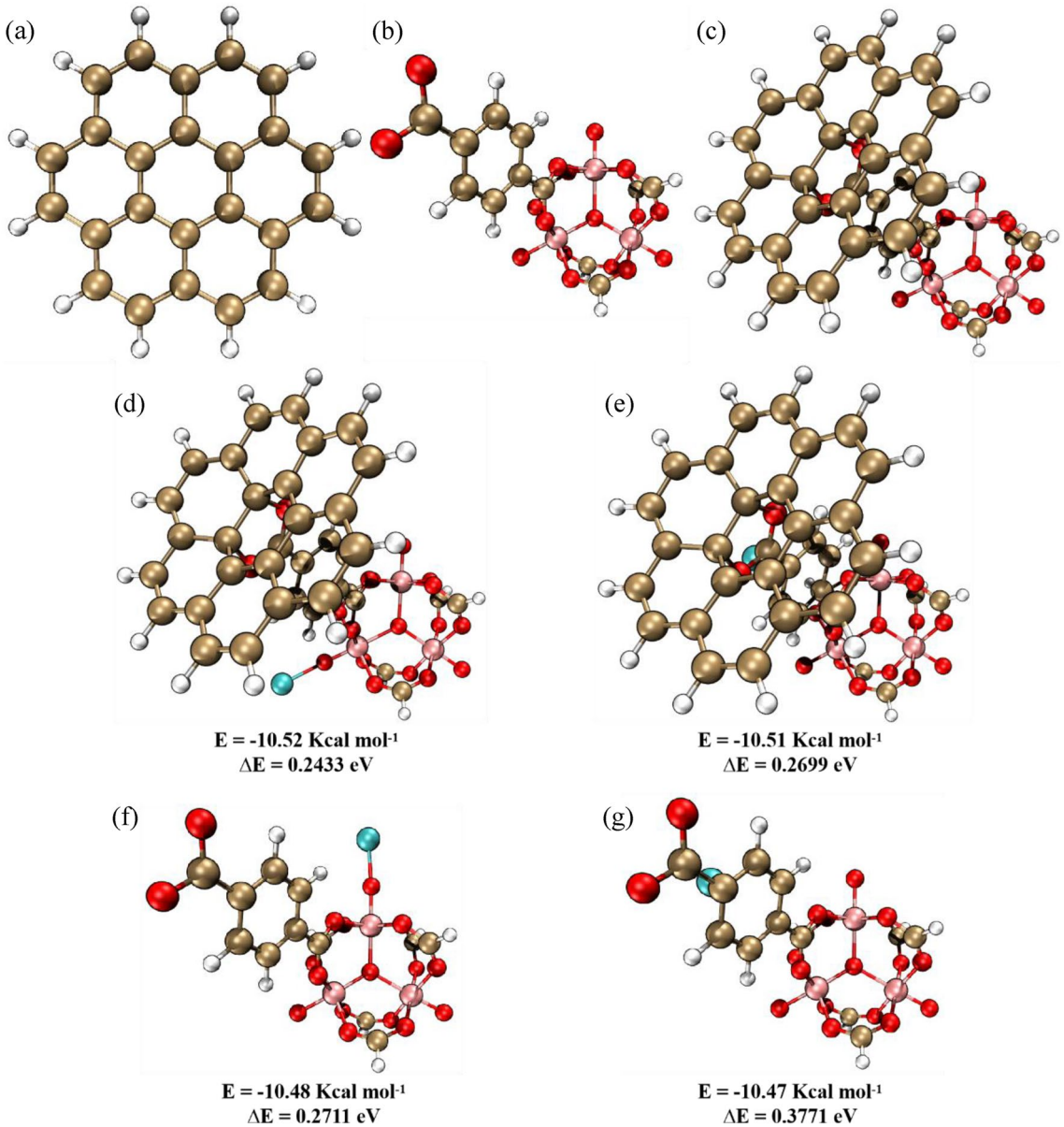


**Fig. 3** Optimized structure of **a** BC, **b** MIL-88b, **c** BC@MIL-88b, adsorption energies of **d**, **e** BC@MIL-88b, and **f**, **g** MIL-88b for $La^{3+}$

Complexation energy, another name for interaction energy, is a crucial quantum chemical term that quantifies the amount of energy needed for a collection of significant atoms to interact with one another or to form complexes (Casella and Saielli 2011). To clarify the type of interactions present in metal adsorbent systems, this parameter might be included while examining the adsorption characteristics of adsorbents (Lawal et al. 2018). According to this study, the total of the separated compounds has a relationship with the interaction energy of the loading procedure. Adsorption energy of $La^{3+}$ on BC was −1.51 kcal $mol^{-1}$. Functionalization of BC with MOF significantly improved the adsorption properties of BC. Figure 3d–g shows the optimum adsorption arrangements for MIL-88b and BC@MIL-88b. The structure was characterized by significantly negative adsorption energy, which suggested that the binding of La to these sites was spontaneous. The corresponding interactions were primarily caused by La–O bond formation and electrostatic attraction of $La^{3+}$ to the benzene ring. Figure 3 shows that the La–O bond was significant and its interaction was more stable. Among them, $La^{3+}$ was adsorbed onto MIL-88b and BC@MIL-88b with interaction energies of −10.48, −10.47, −10.52, and −10.51 kcal $mol^{-1}$, respectively. Therefore, MOF contributes significantly to the adsorption properties of the BC surface.

HOMO and LUMO, via intramolecular charge transfer, offer pertinent information about quantum chemistry (Salahshoori et al. 2024). Estimating the ionisation potential (IP) and electron affinity (EA) will reveal the system's nucleophilic and electron-absorbing capabilities, respectively. Equations (3–10) can be used to calculate the quantum chemical descriptor, which consists of the following: electronegativity (χ), hardness (η), chemical potential (μ), softness (σ), and electrophilicity (ω).

$$\varepsilon = \frac{1}{\omega} \tag{3}$$

$$\eta = \frac{E_{LUMO} - E_{HOMO}}{2} \tag{4}$$

$$\sigma = \frac{1}{\eta} \tag{5}$$

$$\mu = \frac{E_{LUMO} + E_{HOMO}}{2} \tag{6}$$

$$\chi = -\mu \tag{7}$$

$$\omega = \frac{(E_{LUMO} - E_{HOMO})^2}{8\eta} \tag{8}$$

$$EA = -E_{LUMO} \tag{9}$$

$$IP = -E_{HOMO} \tag{10}$$

Estimates of certain quantum chemical properties of selected drugs adsorbed on BC, MIL-88b, and BC@MIL-88b were provided in Table 1. With comparatively lower η and higher σ values, BC@MIL-88b demonstrated superior reactivity compared to solo BC and MIL-88b. This might be the result of MIL-88b's modification of BC, which helps to make the surface of BC softer and less rigid. One consistent finding based on these characteristics reveals that an upward trend in the $\Delta E$ is linked to a decrease in softness, an increase in chemical hardness, and a rise in the electrophilicity index. Changes in electronegativity are what move the electrons, while the hardness parameter serves as a resistor. Compounds with high electrophilic indices display electrophilic behaviour; the global electrophilic index (ω) measures a system's electrophilic power.

Electrostatic potential (ESP) of BC and MIL-88b was also looked at (Fig. 4). The entire electrostatic influence that each atom's charge distribution in a given complex carries with it is known as the ESP. The ESP surface analysis results agreed with the binding site and reactivity expectations. Mapping the net electrostatic charged surfaces of molecules allows one to visually investigate their relative polarity. Different colours are used to designate the electrostatic potential value: the colour blue represents the area with the most negative electrostatic potential, whereas the colour red represents the area with the most positive electrostatic potential. A molecule's concentrated electron density attracts protons when its electrostatic potential is negative. The nucleus's repulsion of protons in areas with low electron density and partial nuclear charge

**Table 1** Quantum chemical descriptors for the sorption process based on DFT

| Adsorbents | $E_{LUMO}$ | $E_{HOMO}$ | $\Delta E$ | EA | IP | $\varepsilon$ | $\eta$ | $\sigma$ | $\mu$ | $\chi$ | $\omega$ |
|---|---|---|---|---|---|---|---|---|---|---|---|
| BC | −1.419 | −5.456 | 4.037 | 1.419 | 5.456 | 0.991 | 2.018 | 0.495 | −3.438 | 3.438 | 1.009 |
| MIL-88b | −5.192 | −7.549 | 2.357 | 5.192 | 7.549 | 1.698 | 1.178 | 0.849 | −6.371 | 6.371 | 0.589 |
| BC@MIL-88b | −4.646 | −5.863 | 1.217 | 4.646 | 5.863 | 3.289 | 0.608 | 1.643 | −5.255 | 5.255 | 0.304 |

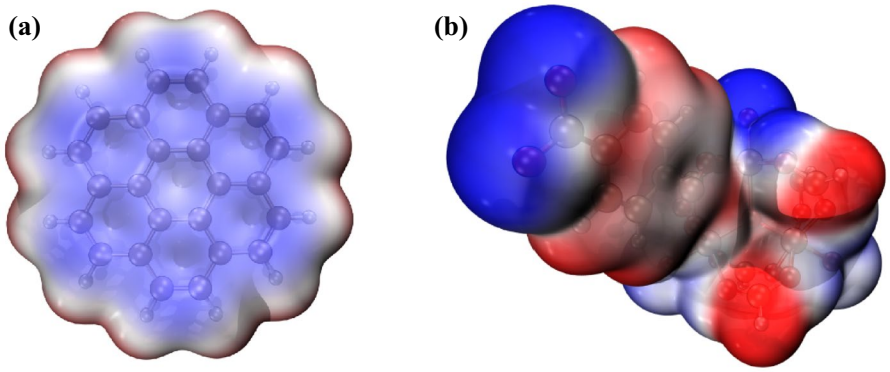


**Fig. 4** Electrostatic potential of **a** BC and **b** MIL-88b

shielding is known as positive electrostatic potential. The surface image is displayed in Fig. 4, and the ESP was computed for this adsorption investigation.

Figure 3g–d also displays the $\Delta E$ of MIL-88b and BC@MIL-88b, with smaller gaps signifying higher electron transport capability and reactivity (Lawal et al. 2020). It could be seen from Fig. 5, for BC, HOMO is an off-domain π orbital that facilitates binding to the target. LUMO is an off-domain π* orbital that affects reactivity with other chemicals. The HOMO value was about −5.4569 eV and the LUMO value was about −1.4195 eV. The organic ligand's benzene ring structure was where most of the HOMO was concentrated in the MIL-88b structure. This ring structure's electronic delocalization within the conjugated system was facilitated by the delocalized π-orbital across the conjugated system, which increased stability. On the other hand, LUMO was mainly found on ketone and ester functional groups that were close to the metal centers and organic ligands. This reactive orbital was affected by nearby organic ligands and metal centers, and it facilitated nucleophilic assault. The LUMO value was around −5.1929 eV, while the HOMO value was approximately −7.5498 eV. While the LUMO was focused on the benzene ring structure of biochar, the HOMO was mainly confined to the metal core of MIL-88b, which was linked to Fe and O atoms in the BC@MIL-88b structure. The HOMO value was about −5.8638 eV and the LUMO value was about −4.6469 eV. Chemical activity and charge transfer of the structures can be determined using $\Delta E$ to determine the gap ($E_{LUMO}$–$E_{HOMO}$). The $\Delta E$ energies of the constituents have a strong correlation with their chemical stability and reactivity. Greater orbital gaps result in less polarization and chemical reactivity in molecules. The efficiency is enhanced by the decreased gap in $\Delta$E values since it takes less energy to extract the electron from the final occupied orbital. BC, MIL-88b, and BC@MIL-88b have $\Delta$E values of 4.0370 eV, 2.3352 eV, and 1.2169 eV, respectively. The $\Delta E$ gap shows a trend of BC<MIL-88b<BC@MIL-88b, suggesting more frequent chemical interactions in BC@MIL-88b. The outcomes showed that ligand exchange and electrostatic attraction may efficiently adsorb $La^{3+}$ on the composite surface. The synergistic impact of ligand exchange and π–π interaction is logical, as the empirical observations align well with the predictions made using Density Functional Theory (DFT).

### 3.3 Adsorption isotherms

After agitating the mixture for 24 h at 298 K and 250 rpm, $La^{3+}$ adsorption isotherms were obtained at starting pH 6.0. Figure 6a displays relative results. Up until equilibrium was attained, the loading capacities of three materials as the $La^{3+}$ concentration rose. At $La^{3+}$ concentrations below 60 mg $L^{-1}$, the adsorption rate rose with accelerated concentration, whereas it dropped higher than 60 mg $L^{-1}$. This is because at low concentrations, the surfaces of BC, MIL-88b and BC@MIL-88b contain enough adsorption sites, with $La^{3+}$ occupying just a tiny percentage of them. As the concentration of $La^{3+}$ grows, it possesses a more powerful driving force to raise the frequency of collisions between $La^{3+}$ ions and adsorption sites and overcome the mass transfer barrier of BC, MIL-88b, and BC@MIL-88b, which improves the adsorption capacity of the above three adsorbents. Finally, the adsorption sites on these three materials were saturated and the adsorption reached equilibrium. The maximum adsorption of $La^{3+}$ on BC, MIL-88b, and BC@MIL-88b reached 146.29 mg $g^{-1}$, 165.55 mg $g^{-1}$, and 288.89 mg $g^{-1}$ at 298 K, respectively.

Notably, the $La^{3+}$ loading capacities of similar materials (Table S4) were considerably lower than that of BC@MIL-88b. To further investigate the process underlying the loading characteristics of

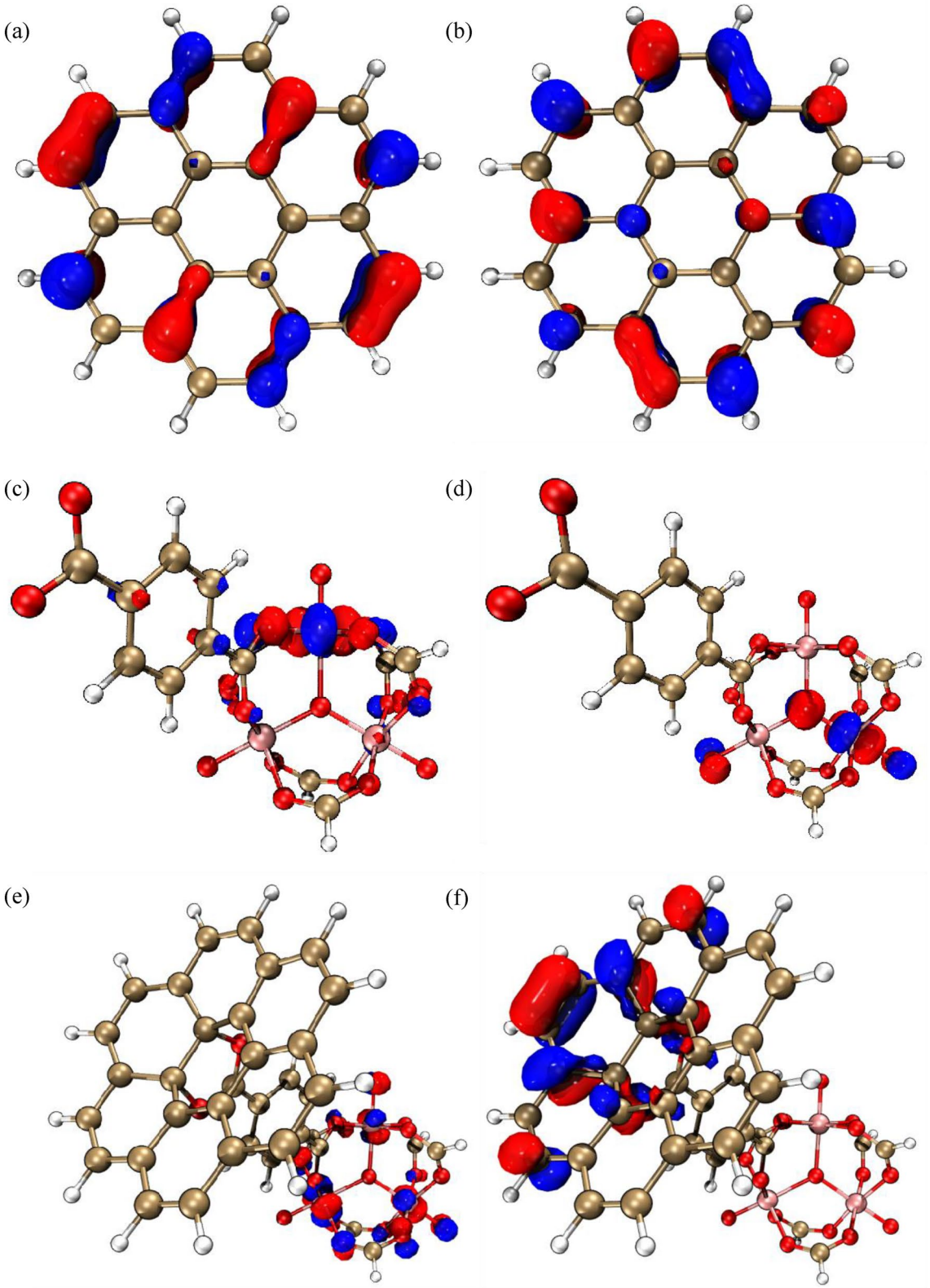


**Fig. 5** HOMO orbital diagrams of **a** BC, **c** MIL-88b, **e** BC@MIL-88b and LUMO orbital diagrams of **b** BC, **d** MIL-88b, and **f** BC@MIL-88b

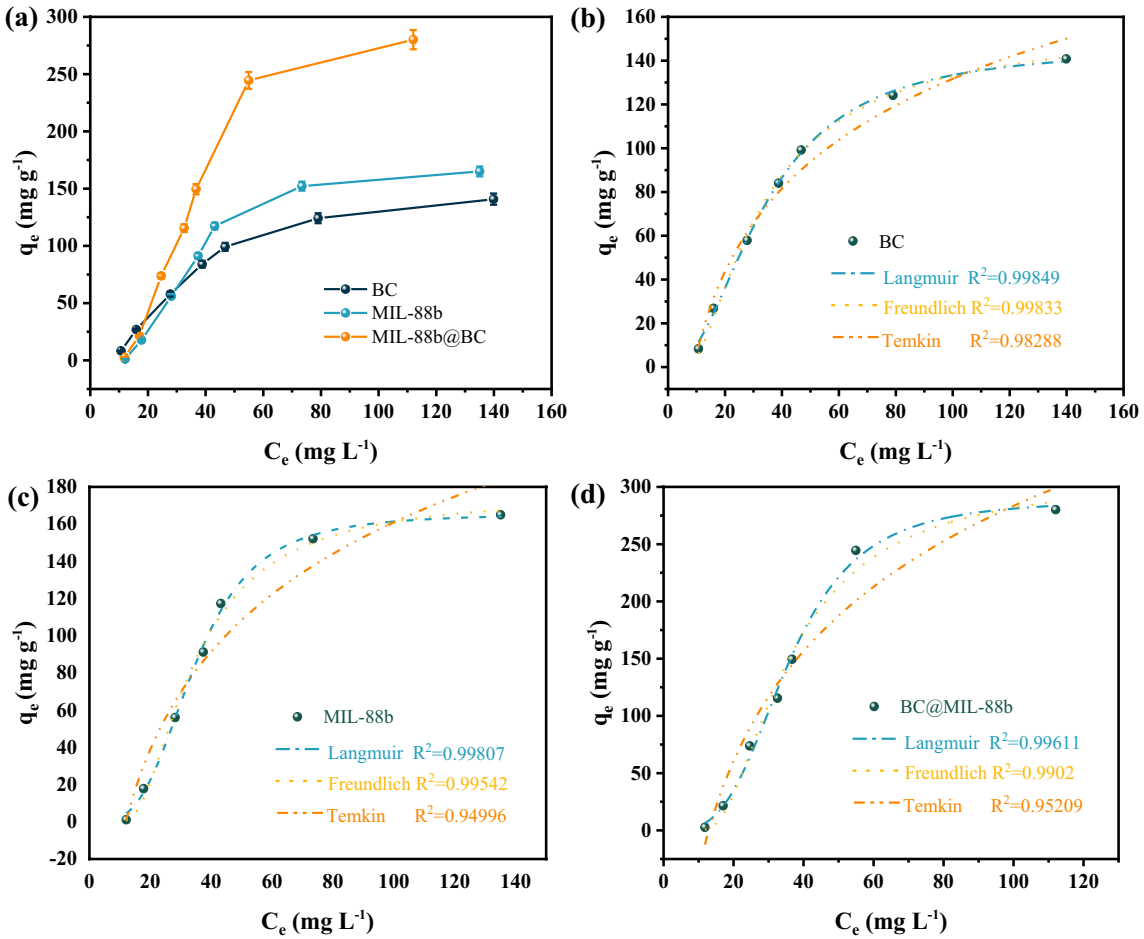


**Fig. 6** **a** Adsorption isotherms; Langmuir, Freundlich, and Temkin models of **b** BC, **c** MIL-88b and **d** BC@MIL-88b

three adsorbents on $La^{3+}$, we investigated the BC, MIL-88b, and BC@MIL-88b adsorption isotherms using the Freundlich, Langmuir, and Temkin models. (Fig. 6b–d), and Eqs. (3)–(5) are shown in Text S5 (Huang et al. 2022). The three models' fitting coefficients ($R^2$) at 298 K showed the following order: Langmuir > Freundlich > Temkin. The outcomes demonstrated that Langmuir model was consistent with the loading process of $La^{3+}$ by three adsorbents. Hence, the adsorption of $La^{3+}$ on the three materials may be accurately characterized using the Langmuir model. The Langmuir model parameter $R_L$ denotes the favorability of adsorption (Eq. (6)). (Tang et al. 2021):

$$R_L = \frac{1}{1 + K_L C_0} \tag{11}$$

where $C_0$ is the starting $La^{3+}$ concentration and $K_L$ is the Langmuir equilibrium constant.

Conditions that are either favourable or unfavourable are indicated by $R_L$ values of 0–1 and >1, respectively. Herein, the $R_L$ values of BC, MIL-88b, and BC@MIL-88b (Table S5) were below 1, showing favorable adsorption. The Temkin model's $B_T$ values were positive, as Table S4 demonstrates, suggesting that the adsorption of $La^{3+}$ was exothermic.

### 3.4 Adsorption kinetics

One important component affecting the loading process is reaction time. Here, at a temperature of 298 K and an agitation rate of 250 rpm, the effect of reaction duration (3–600 min) on the loading of $La^{3+}$ (60 mg $L^{-1}$) on BC, MIL-88b, and BC@MIL-88b was examined. Every time an adsorption equilibrium was attained, the adsorption capacity rose over time and stabilized above a particular threshold (Fig. 7a). As can be seen from the figure, the

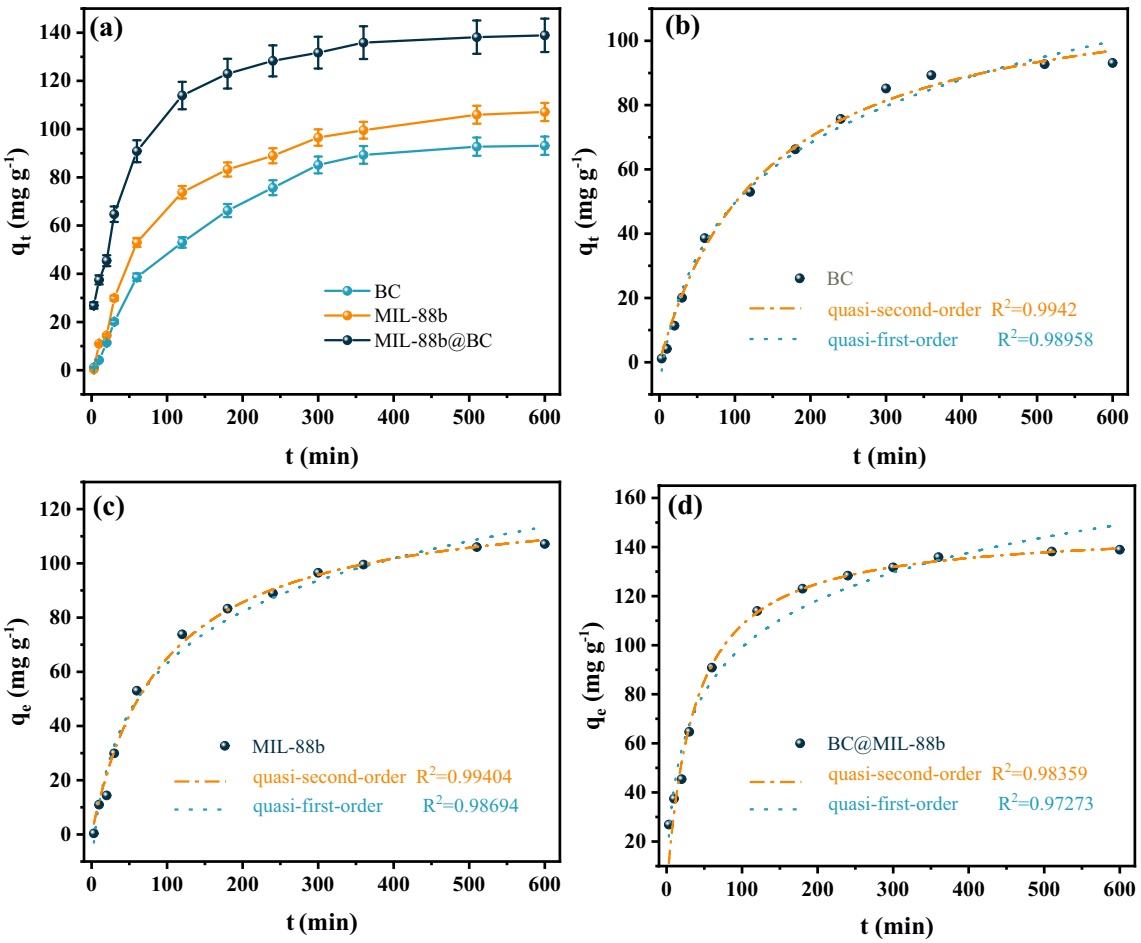


**Fig. 7** **a** Influences of time on the adsorption; kinetic models of **b** BC, **c** MIL-88b and **d** BC@MIL-88b

adsorption basically reached equilibrium when the reaction time reached 6 h, and the subsequent adsorption experiments were all completed in the adsorption equilibrium time. The adsorption kinetics were fitted using internal diffusion, pseudo-second-order, and pseudo-first-order models (Ji et al. 2024). The following are the equations for these models:

$$q_t = q_e(1 - e^{-k_1 t}) \tag{12}$$

$$q_t = \frac{q_e^2 k_2 t}{1 + q_e k_2 t} \tag{13}$$

$$q_t = k_i t^{0.5} + C \tag{14}$$

where C (mg g$^{-1}$) is a constant associated with the liquid sheet's thickness and $k_1$ (min$^{-1}$), $k_2$ (g mg$^{-1}$ min$^{-1}$), and $k_i$ (mg g$^{-1}$ min$^{0.5}$) are the adsorption rate constants for the pseudo-first-order, pseudo-second-order, and internal diffusion models, respectively.

The dynamic model's factors are listed in Table S6, and the fitting models are shown in Fig. 7b–d. For BC, MIL-88b, and BC@MIL-88b, the fitting coefficients $R^2$ showed a pseudo-second-order > pseudo-first-order hierarchy. The pseudo-second-order model's estimated $q_e$ values for each of the three adsorbents showed strong concordance with the experimental data. As a result, the pseudo-second-order model provided the best description of the $La^{3+}$ adsorption kinetics and suggested that chemisorption was involved in the process. Fig. S2 shows the internal diffusion models used for the three adsorbents. The internal diffusion model featured three stages corresponding to adsorption processes involving multiple diffusion mechanisms. In the first stage (0–30 min, Fig. 7d), the maximum adsorption rates of BC, MIL-88b, and BC@MIL-88b were 6.42464, 8.74556, and 10.8674 mg g$^{-1}$ min$^{0.5}$, respectively, and the main event was membrane diffusion. In the second (gradual

adsorption) stage (30–300 min), these rates decreased to 4.67171, 4.05375, and 3.79929 mg $g^{-1}$ $min^{0.5}$, respectively. The third step involved the establishment of an adsorption equilibrium. The fact that the linear segments in Figure S2 do not cross at the origin suggests that a number of kinetic mechanisms, including intrapore diffusion, surface adsorption and external mass transfer, as well as intramaterial diffusion affect the adsorption processes on the three adsorbents.

### 3.5 Thermodynamics

The $La^{3+}$ adsorption capacity was observed to be favourably linked with temperature (298–328 K) (Fig. S3a). Calculating the standard entropy change ($\Delta S^0$), Gibbs free energy change ($\Delta G^0$), and standard enthalpy change ($\Delta H^0$) of $La^{3+}$ adsorption provided further information (Text S6). Fig. S3b displays the correlation between ln *k* and *1/T*, while Table S7 lists the parameters of the corresponding linear fit. The positive $\Delta H^0$ value suggested that the adsorption was endothermic and, hence, promoted by high temperatures. The degree of disorder at the solid–liquid interface increased following adsorption, as indicated by the positive value of $\Delta S_0$, whereas the negative $\Delta G0$ value revealed that $La^{3+}$ adsorption was spontaneous (Gu et al. 2017). Therefore, the adsorption of $La^{3+}$ was temperature sensitive.

### 3.6 Effects of pH

The solution pH affects the state of $La^{3+}$ ions in aqueous media and thus strongly influences their adsorption (Wang et al. 2015). Figure 8a shows the distribution of La species over a broad pH range, revealing a sharp decrease in the concentration of $La^{3+}$ and formation of insoluble $La(OH)_3$ at pH > 6. Therefore, it was determined that the pH of the solution is a significant impact. Fig. S4 shows the zeta potentials of BC@MIL-88b at pH 1–11, demonstrating that at pH < 10.58, the adsorbent surface was positively charged. This positive charge hindered the adsorption of $La^{3+}$ because of electrostatic repulsion (Qu et al. 2024b). Therefore, the adsorption mechanism needs to be further explored and elucidated in addition to the electrostatic interactions.

The effects of pH (1–6) on the three adsorbents' $La^{3+}$ adsorption capacity, which was evaluated at $C_0 = 60$ mg $L^{-1}$, are displayed in Fig. 8b. In acidic water, numerous active sites remained protonated, which prevented the adsorption of $La^{3+}$ and reduced the adsorption capacity. At neutral pH, $La^{3+}$ replaced more protons at the active sites, which resulted in an increased adsorption capacity. The competition for adsorption decreases (Xie et al. 2023). Moreover, high pH favored the deprotonation of organic ligands, increasing their ability to bind metal cations and, hence, adsorption capacity. As the adsorption saturation point was reached, the adsorption capacity remained relatively constant with increasing pH. Given that the $La^{3+}$ adsorption capacity peaked at pH 6, this pH was selected for subsequent experiments. The electron cloud in the aromatic ring of the organic ligand, terephthalic acid, strongly interacted with the $La^{3+}$ ions, leading to their adsorption via electrostatic attraction (Jiang et al. 2016).

To ascertain whether MIL-88b and BC@MIL-88b will produce secondary contamination in aquatic ecosystems, the structural stabilities of these compounds were investigated by quantifying the quantity of remaining metal ions in the solution following adsorption. According to Table S8, the concentration of $Fe^{3+}$ in the solution was nearly negligible at pH 3.0–6.0 and was well below the 0.3 mg $L^{-1}$ level specified in the Chinese

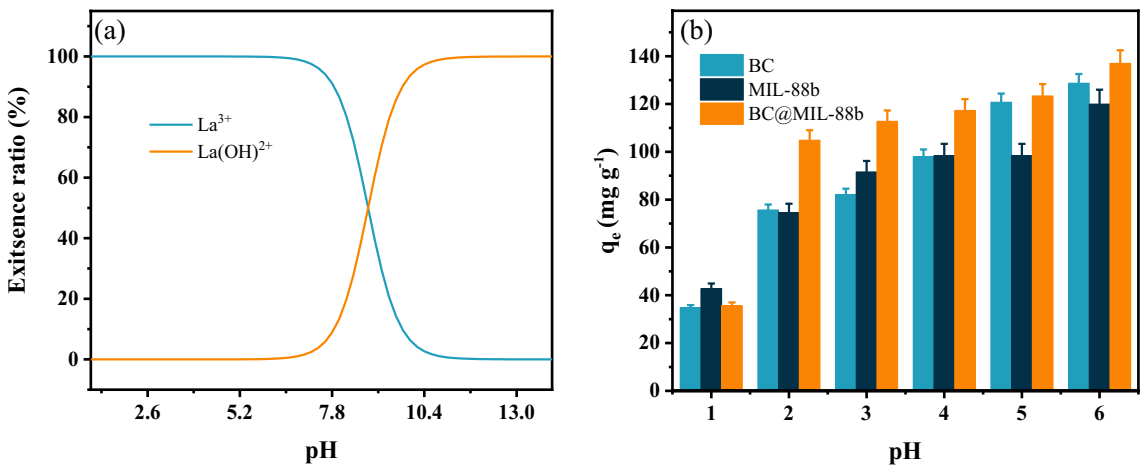


**Fig. 8** **a** La species with a wide pH range, **b** effect of the solution pH on the adsorption capacities

Drinking Water Sanitation Standard (GB5749-2006). Therefore, MIL-88b and BC@MIL-88b were concluded to be ecofriendly in real-life applications. These findings validated the structural stabilities of MIL-88b and BC@MIL-88b, highlighting their significant potential for adsorptive recovery applications.

### 3.7 Effects of coexisting ions

Adsorbent selectivity is essential for their real-world uses. One should reduce the impacts of various cations on the adsorption process due to the complexity and variety of the ambient circumstances. The selectivities of BC@MIL-88b for $La^{3+}$ were tested using $Tb^{3+}$, $Y^{3+}$, $Lu^{3+}$, $Ce^{3+}$, $A1^{3+}$, $Fe^{3+}$, $Na^{+}$, $K^{+}$, $Ca^{2+}$, and $Mg^{2+}$ as interfering cations at a concentration of $La^{3+}$of 60 mg $L^{-1}$ and interferent concentrations of 10, 20, and 40 mg $L^{-1}$ (Fig. S5a). The effect of metal ions on the adsorption of $La^{3+}$ by BC and MIL-88b is shown in Fig. S5b, c. $Ce^{3+}$, $A1^{3+}$, $Fe^{3+}$, $Na^{+}$, $K^{+}$, $Ca^{2+}$, $Mg^{2+}$ did not markedly interfere with the adsorption of BC@MIL-88b for $La^{3+}$, whereas $Tb^{3+}$, $Y^{3+}$, and $Lu^{3+}$ had detrimental effects on $La^{3+}$ adsorption, with higher concentrations resulting in stronger interference. The concentrations of $Tb^{3+}$, $Y^{3+}$, and $Lu^{3+}$ in natural samples are typically considerably lower than those used herein. Notably, the adsorption efficiency of REEs increases with their decreasing ionic radius because of the concomitant increase in the strength of REE ion binding by the adsorbent (Liang and Zeng 2024). Consequently, we concluded that the three adsorbents exhibited robust anti-interference capabilities and effectively extracted $La^{3+}$ from wastewater in the presence of competing species.

### 3.8 Application to real-life samples

To evaluate the practical application of BC, MIL-88b, and BC@MIL-88b, water samples were analyzed. Fig. S6a reveals that with the increasing adsorbent loading, the concentration of $La^{3+}$ in the overland runoff rapidly decreased until equilibrium was reached. While there are no precise maximum permitted limits for REEs in drinking water (Balaram 2019), ecotoxicological calculations indicate that 10.1 ng $mL^{-1}$ of $La^{3+}$ is the highest allowed concentration in drinking water (Al Momani et al. 2023). The loading on $La^{3+}$ reached equilibrium when the dose of BC@MIL-88b reached 0.2 g $L^{-1}$. In contrast, the dose of MIL-88b did not saturate the load on $La^{3+}$ even at 1.0 g $L^{-1}$. The adsorbent loading could possibly be increased further according to the trend shown in the figure; however, this would also increase treatment costs. The superior performance of BC@MIL-88b demonstrated the advantages of this composite over its precursors and confirmed its applicability in complex environments. The adsorption capability of BC for $La^{3+}$ is maximal at low concentrations, as shown in Fig. S4a, consistent with the findings of the adsorption isothermal experiment.

### 3.9 Absorbent regeneration

The recyclability of BC@MIL-88b was examined at 298 K using 0.05 M HCl as an eluent (Fig. S6b). After four reuse cycles, BC@MIL-88b maintained an adsorption rate of >93% for a 5 mg $L^{-1}$ $La^{3+}$ solution, with the desorption rate exceeding 80% in all cycles until the final cycle. This adsorbent was structurally stable and well suited for practical applications. The SEM patterns of spent BC@MIL-88b (Fig. S8) indicated that recycling had no impact on its basic framework, indicating that the adsorbent structure was stable. The efficient regeneration and reuse of BC@MIL-88b demonstrated the high practical value of this adsorbent for $La^{3+}$ removal from aqueous media.

### 3.10 Dynamic adsorption experiment

By using fixed-bed column tests to mimic the dynamic adsorption process, the usefulness of BC@MIL-88b was examined. It is evident from Fig. S7 that bed decay was achieved within 540 min, indicating that BC@MIL-88b has a strong affinity for $La^{3+}$. This dynamic process was examined using the Thomas and Yoon–Nelson model, see Eqs. (12), (13).

$$\ln\left(\frac{C_0}{C_t}-1\right)=\frac{K_{Th}}{Q}(q_{0th}X-C_0t) \tag{15}$$

$$ln\left(\frac{C_t}{C_0-C_t}\right)=K_{NY}t-\tau K_{NY} \tag{16}$$

where X (g) is the weight of BC@MIL-88b, Q (mL $min^{-1}$) is the flow rate, $K_{Th}$ (mL $min^{-1}$ $mg^{-1}$) is the Thomas constant, and $q_{0th}$ (mg $g^{-1}$) is the maximal adsorption capacity. The Yoon–Nelson constant is $K_{YN}$ ($min^{-1}$) while the time needed for a 50% breakthrough is τ (min).

A kinetic model for column adsorption, the Thomas model is primarily used to assess permeation curves and compute column performance in adsorption. The Langmuir model of the adsorption process is assumed to be followed by the model. The derivation's primary drawback is its reliance on second-order kinetics. Moreover, interfacial mass transfer, not chemical processes, controls adsorption (Delgado et al. 2006). Typically, the Yoon–Nelson kinetic model is used to analyze a solution's ionic concentration range between saturation and burst times. This is predicated on the idea

**Table 2** Column experimental model parameters

| Yoon–Nelson | | | | Thomas | | |
|---|---|---|---|---|---|---|
| **Adsorbates** | **$K_{YN}$ ($min^{-1}$)** | **τ(min)** | **$R^2$** | **$K_{Th}$ ($mL\ min^{-1}\ mg^{-1}$)** | **$q_{0th}$ ($mg\ g^{-1}$)** | **$R^2$** |
| $La^{3+}$ | 0.0126 | 345.144 | 0.977 | 1.782 | 121.839 | 0.988 |

that it is feasible to decrease each pollutant molecule's rate of adsorption in proportion to the rate at which the adsorbent ruptures and the pace at which adsorption occurs (Chu 2020).

Table 2 shows the relevant fitted data for the column experiments, and the $R^2$ values demonstrate the applicability of both models to the $La^{3+}$ adsorption process. From the table the τ value represents the time required for 50% contaminant breakthrough in the Yoon–Nelson model. In this study, the breakthrough time takes 345 min. The Thomas model fitted well the adsorption of BC@MIL-88b under fixed bed with $q_{0th} = 121\ mg\ g^{-1}$. The good dynamic adsorption experimental results and low treatment cost proved the suitability of BC@MIL-88b for the recovery of low concentration of $La^{3+}$, which is promising, economically viable and cost-effective.

### 3.11 Adsorption mechanism

As Fig. S8 illustrates, the adsorbed $La^{3+}$ was uniformly distributed on the surface of BC@MIL-88b, which, in combination with Fig. 1, showed a clear homogeneity before adsorption, with both isolated particles and aggregates resulting from particle stacking. These structures showed characteristic nanorod shapes. Throughout the adsorption process, the morphology of BC@MIL-88b gradually transited to a more rounded

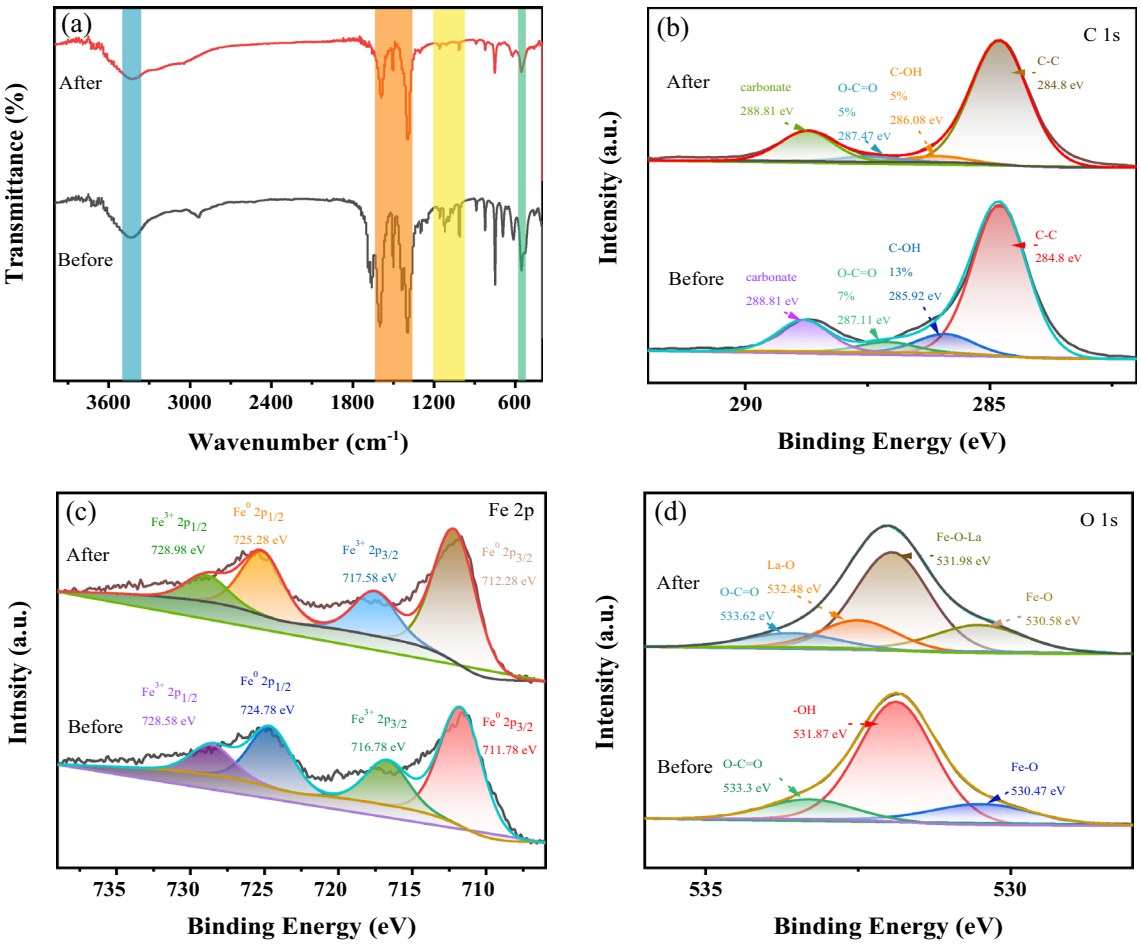


**Fig. 9** **a** FTIR spectra and **b** C 1s, **c** Fe 2p, **d** O 1s of BC@MIL-88b before and after adsorption for XPS analysis

shape with granular protrusions, demonstrating a characteristic stacking that resulted in aggregates with granular protrusions on their surface and a reduction in the unique nanorods' clarity, which suggested that the rare earth elements were adsorbed on the surface of BC@MIL-88b, leading to a change in morphology. Furthermore, it was found that the La-loaded crystals had a flocculant layer adhered to their surface. Due to its 0.27% $La^{3+}$ content, the material was able to transfer $La^{3+}$ and lodge in micropores with efficiency.

FTIR spectroscopy was utilized to analyze the adsorption-induced changes in the adsorbent functional groups and study their interactions (Figs. 9a and S9). The FTIR spectrum of pristine BC@MIL-88b (Fig. 9a) displayed a distinctive O–H peak at 3436.51 $cm^{-1}$ as well as carboxyl C–O peaks at 1682.84 $cm^{-1}$ (asymmetric stretch) and 1393.88 $cm^{-1}$ (symmetric stretch). The peaks at 1500–1600 $cm^{-1}$ were ascribed to the stretching vibrations of the benzene ring skeleton, while those at 1297.82 $cm^{-1}$ and 1157.53 $cm^{-1}$ corresponded to C–O–C moieties. The peak appearing at 500–700 $cm^{-1}$ is attributed to the Fe–O group, and after adsorption, the relative intensity of the peak at 555.48 $cm^{-1}$ is significantly reduced, which can be explained by the coordination between Fe–O and $La^{3+}$. The peak at 3392.27 $cm^{-1}$ lost intensity after adsorption, which demonstrates that $La^{3+}$ was adsorbed through the substitution of hydroxyl groups rather than by direct binding to Fe. The change in the peaks at 1500–1600 $cm^{-1}$ indicated the participation of the benzene ring structure in the adsorption of $La^{3+}$. Thus, we concluded that during the adsorption process, hydroxyl groups were substituted by $La^{3+}$ via ligand exchange to create Fe–O–La bonds, which agrees with the results of adsorption kinetics experiments.

The mechanism of $La^{3+}$ adsorption was further probed by XPS. The Fe 2p spectrum showed characteristic Fe $2p_{1/2}$ peaks at 728.58 eV and 724.78 eV as well as Fe $2p_{3/2}$ peaks at 716.78 eV and 711.78 eV (Tong et al. 2022). The above peaks were redshifted to 728.98 eV, 725.28 eV, 717.58 eV, and 712.28 eV following adsorption, which suggested electron transfer in the 2p valence band of Fe (potentially resulting from the replacement of functional groups in the adsorbent). This modification modified the chemical milieu surrounding Fe, suggesting that internal Fe–O–La complexes could be formed) (He et al. 2017; Feng et al. 2022). The O 1s spectrum featured Fe–O (530.47 eV), –OH (531.87 eV), and O–C=O (533.3 eV) peaks. After adsorption, the –OH peak vanished and was replaced by the propranolol peaks of Fe–O–La (531.98 eV) and La–O (532.48 eV) (Li et al. 2023). The C 1s spectrum featured C–C (284.8 eV), C–OH (285.92 eV), O–C=O (287.11 eV), and carbonate (288.81 eV) peaks. Following adsorption, the C–OH and O–C=O peaks shifted, and their areal percentages decreased from 13% to 5% and 7% to 5%, respectively. Thus, the reactive –OH groups could be substituted by La to form internal Fe–O–La complexes through ligand exchange and adsorb $La^{3+}$. These results agreed with those of FTIR spectroscopy.

## 4 Conclusions

A novel BC-MOF composite was synthesized and validated by practical experiments based on the relevant theoretical basis obtained from theoretical calculations, which proved that its adsorption performance for $La^{3+}$ was significant and significantly better than that of the parent BC and MOF, and was used to recover lanthanum from surface runoff around the Jiangxi Rare Earth Mining Area both directly and selectively. The strong electrostatic attraction of the benzene ring and the creation of Fe–O–La coordination bonds by $La^{3+}$ through the substitution of hydroxyl groups were credited with this outstanding performance, which were the main factors for the ultra-high adsorption of $La^{3+}$ at pH 6. In addition, BC@MIL-88b can be regenerated by rinsing with dilute hydrochloric acid without changing the crystal structure. In continuous adsorption experiments, BC@MIL-88b exhibited excellent bed decay time (540 min). Thus, BC@MIL-88b is considered a highly robust material for the adsorptive recovery of $La^{3+}$ from wastewater in various environments. The in-depth look at a new way to treat wastewater using biochar modified with a metal-organic framework in this study shows that it could work well and reduce pollution for a long time. This study heralds a transformative shift toward cleaner, more resource-efficient water management practices, demonstrating the enormous potential for scalable, cost-effective, and environmentally friendly solutions. We will need more cooperation and implementation to achieve a sustainable future.

## Supplementary Information

The online version contains supplementary material available at https://doi.org/10.1007/s42773-024-00419-x.

Additional file 1.

**Acknowledgements**

This work was financially supported by the International Science & Technology Innovation Program of Chinese Academy of Agriculture Science (CAAS-CFSGLCA-IEDA-202302 and CAAS-ZDRW202110), Basic Scientific Research Project of Liaoning Provincial Department of Education (JYTMS20230179) and the Young Scientist Exchange Programme between the People's Republic of China and the Republic of Korea. The authors additionally acknowledge Hongzhiwei's assistance with technical communication support and computer time support.

**Author contributions**

Qilan Huang: Material preparation, Data collection and analysis, Writing-Original draft; Qianru Zhang: Writing-Review & editing, Supervision, Conceptualization, Project administration; Shuwen Zhao: Formal analysis,

Data curation; Chuchen Zhang: Visualization, Data curation; Huixin Guan: Material preparation, Data collection and analysis; Jianqiao Liu: Supervision, Conceptualization.

**Funding**
This work was financially supported by the International Science & Technology Innovation Program of Chinese Academy of Agriculture Science (CAAS-CFSGLCA-IEDA-202302 and CAAS-ZDRW202110), Basic Scientific Research Project of Liaoning Provincial Department of Education (JYTMS20230179) and the Young Scientist Exchange Programme between the People's Republic of China and the Republic of Korea.

**Data availability**
The datasets used or analyzed during the study are available from the corresponding author on reasonable request.

## Declarations

**Competing interests**
The authors declare that they have no known competing financial interests or personal relationships that could have appeared to influence the work reported in this paper.

**Author details**
[1]State Key Laboratory of Efficient Utilization of Arid and Semi−arid Arable Land in Northern China, Institute of Agricultural Resources and Regional Planning, Chinese Academy of Agricultural Sciences, Haidian District, No. 12 South Zhongguancun Street, Beijing 100081, China. [2]College of Information Science and Technology, Dalian Maritime University, No. 1 Linghai Road, Dalian 116026, China.

Received: 16 July 2024 Revised: 20 December 2024 Accepted: 22 December 2024
Published online: 08 February 2025

**References**

Abdel-Magied AF, Abdelhamid HN, Ashour RM, Zou X, Forsberg K (2019) Hierarchical porous Zeolitic Imidazolate frameworks nanoparticles for efficient adsorption of rare-earth elements. Microporous Mesoporous Mater 278:175–184. https://doi.org/10.1016/j.micromeso.2018.11.022

Al Momani DE, Al Ansari Z, Ouda M, Abujayyab M, Kareem M, Agbaje T, Sizirici B (2023) Occurrence, treatment, and potential recovery of rare earth elements from wastewater in the context of a circular economy. J Water Proc Eng 55:104223. https://doi.org/10.1016/j.jwpe.2023.104223

Balaram V (2019) Rare earth elements: a review of applications, occurrence, exploration, analysis, recycling, and environmental impact. Geosci Front 10(4):1285–1303. https://doi.org/10.1016/j.gsf.2018.12.005

Binnemans K, Jones PT, Blanpain B, Van Gerven T, Yang Y, Walton A, Buchert M (2013) Recycling of rare earths: a critical review. J Clean Prod 51:1–22. https://doi.org/10.1016/j.jclepro.2012.12.037

Borges GA, Dias Ferreira GM, Felix Siqueira KP, Dias A, Najera Navarro KO, Barros e Silva SJ, Rodrigues GD, Mageste AB (2020) Adsorption of organic and inorganic arsenic from aqueous solutions using mgal-ldh with incorporated nitroprusside. J Colloid Interface Sci 575:194–205. https://doi.org/10.1016/j.jcis.2020.04.078

Casella G, Saielli G (2011) Dft study of the interaction free energy of Π-Π complexes of fullerenes with Buckybowls and Viologen Dimers. New J Chem 35(7):1453–1459. https://doi.org/10.1039/c1nj20117d

Chakhtouna H, Benzeid H, Zari N, Qaiss A, Bouhfid R (2021) Functional Cofe2O4-modified biochar derived from banana pseudostem as an efficient adsorbent for the removal of amoxicillin from water. Sep Purif Technol 266:118592. https://doi.org/10.1016/j.seppur.2021.118592

Chakhtouna H, Benzeid H, Zari N, Qaiss A, Bouhfid R (2023) Microwave-assisted synthesis of Mil-53(Fe)/biochar composite from date palm for ciprofloxacin and ofloxacin antibiotics removal. Sep Purif Technol 308:122850. https://doi.org/10.1016/j.seppur.2022.122850

Chen T, Cao G, Qiang Y, Lu Y, Qin R, Xu W, Xie Y, Mao R (2024) Effective removal of Pb (Ii) from wastewater by zinc-iron bimetallic oxide-modified walnut shell biochar: a combined experimental and Dft calculation approach. J Environ Manage 370:122757. https://doi.org/10.1016/j.jenvman.2024.122757

Chu KH (2020) Breakthrough curve analysis by simplistic models of fixed bed adsorption: in defense of the century-old Bohart-Adams model. Chem Eng J 380:122513. https://doi.org/10.1016/j.cej.2019.122513

Delgado JA, Uguina MA, Sotelo JL, Ruíz B (2006) Fixed-bed adsorption of carbon dioxide-helium, nitrogen-helium and carbon dioxide-nitrogen mixtures onto silicalite pellets. Sep Purif Technol 49(1):91–100. https://doi.org/10.1016/j.seppur.2005.08.011

Deng Y, Liu S, Fu L, Yuan Y, Zhao A, Wang D, Zheng H, Ouyang L, Yuan S (2023) Crystal plane induced metal-support interaction in Pd/Pr-Ceo<Sub>2</Sub> catalyst boosts H<Sub>2</Sub>O-assisted co oxidation. J Catal 417:60–73. https://doi.org/10.1016/j.jcat.2022.11.026

Devic T, Serre C (2014) High valence 3p and transition metal based mofs. Chem Soc Rev 43(16):6097–6115. https://doi.org/10.1039/c4cs00081a

Du L, Ahmad S, Liu L, Wang L, Tang J (2023) A review of antibiotics and antibiotic resistance genes (Args) adsorption by biochar and modified biochar in water. Sci Total Environ 858:159815. https://doi.org/10.1016/j.scitotenv.2022.159815

Ecer U, Yilmaz S (2024) Fabrication of magnetic biochar-Mil-68(Fe)-supported cobalt composite material toward the catalytic reduction performance of crystal violet. J Water Proc Eng 57:104574. https://doi.org/10.1016/j.jwpe.2023.104574

Edahbi M, Plante B, Benzaazoua M (2019) Environmental challenges and identification of the knowledge gaps associated with ree mine wastes management. J Clean Prod 212:1232–1241. https://doi.org/10.1016/j.jclepro.2018.11.228

Feng L, Zhang Q, Ji F, Jiang L, Liu C, Shen Q, Liu Q (2022) Phosphate removal performances of layered double hydroxides (Ldh) embedded polyvinyl alcohol / lanthanum alginate hydrogels. Chem Eng J 430:132754. https://doi.org/10.1016/j.cej.2021.132754

Gu Y, Xie D, Ma Y, Qin W, Zhang H, Wang G, Zhang Y, Zhao H (2017) Size modulation of zirconium-based metal organic frameworks for highly efficient phosphate remediation. ACS Appl Mater Interfaces 9(37):32151–32160. https://doi.org/10.1021/acsami.7b10024

Han J, Song Y, Li H, Wang Y, Zhang L, Sun P, Fan J, Li Y (2023) Preparation of novel magnetic porous biochar and its adsorption mechanism on cerium in rare earth wastewater. Ceram Int 49(6):9901–9908. https://doi.org/10.1016/j.ceramint.2022.11.165

He Y, Lin H, Dong Y, Wang L (2017) Preferable adsorption of phosphate using lanthanum-incorporated porous zeolite: characteristics and mechanism. Appl Surf Sci 426:995–1004. https://doi.org/10.1016/j.apsusc.2017.07.272

Huang C, Huang B, Dong Y, Chen J, Wang Y, Sun X (2017) Efficient and sustainable regeneration of bifunctional ionic liquid for rare earth separation. ACS Sustain Chem Eng 5(4):3471–3477. https://doi.org/10.1021/acssuschemeng.7b00159

Huang Q, Zhao L, Zhu G, Chen D, Ma X, Yang X, Wang S (2022) Outstanding performance of thiophene-based metal-organic frameworks for fluoride capture from wastewater. Sep Purif Technol 298:121567. https://doi.org/10.1016/j.seppur.2022.121567

Hudcová B, Fein JB, Tsang DCW, Komárek M (2022) Mg-Fe Ldh-coated biochars for Metal(Loid) removal: surface complexation modeling and structural change investigations. Chem Eng J 432:134360. https://doi.org/10.1016/j.cej.2021.134360

Iftekhar S, Srivastava V, Sillanpaa M (2017a) Enrichment of lanthanides in aqueous system by cellulose based silica nanocomposite. Chem Eng J 320:151–159. https://doi.org/10.1016/j.cej.2017.03.051

Iftekhar S, Srivastava V, Sillanpaa M (2017b) Synthesis and application of Ldh intercalated cellulose nanocomposite for separation of rare earth elements (Rees). Chem Eng J 309:130–139. https://doi.org/10.1016/j.cej.2016.10.028

Jahan I, Islam MA, Rupam TH, Palash ML, Rocky KA, Saha BB (2022) Enhanced water sorption onto bimetallic Mof-801 for energy conversion applications. Sustain Mater Technol 32:e00442. https://doi.org/10.1016/j.susmat.2022.e00442

Ji X, Liu Y, Gao Z, Lin H, Xu X, Zhang Y, Zhu K, Zhang Y, Sun H, Duan J (2024) Efficiency and mechanism of adsorption for imidacloprid removal from water by Fe-Mg Co-modified water hyacinth-based biochar: batch adsorption fixed-bed adsorption, and Dft calculation. Sep Purif Technol 330:125235. https://doi.org/10.1016/j.seppur.2023.125235

Jiang L, Zhang W, Luo C, Cheng D, Zhu J (2016) Adsorption toward trivalent rare earth element from aqueous solution by zeolitic imidazolate frameworks. Ind Eng Chem Res 55(22):6365–6372. https://doi.org/10.1021/acs.iecr.6b00422

Kim JY, Kim KY, Kim SM, Choi Y-E (2022) Use of rare earth element (Ree)-contaminated acidic water as *Euglena Gracilis* growth stimulator: a strategy for bioremediation and simultaneous increase in biodiesel productivity. Chem Eng J 445:136814. https://doi.org/10.1016/j.cej.2022.136814

Lawal IA, Lawal MM, Akpotu SO, Azeez MA, Ndungu P, Moodley B (2018) Theoretical and experimental adsorption studies of sulfamethoxazole and ketoprofen on synthesized ionic liquids modified Cnts. Ecotoxicol Environ Saf 161:542–552. https://doi.org/10.1016/j.ecoenv.2018.06.019

Lawal IA, Lawal MM, Akpotu SO, Okoro HK, Klink M, Ndungu P (2020) Noncovalent graphene oxide functionalized with ionic liquid: theoretical, isotherm, kinetics, and regeneration studies on the adsorption of pharmaceuticals. Ind Eng Chem Res 59(11):4945–4957. https://doi.org/10.1021/acs.iecr.9b06634

Li K, Gao Q, Yadavalli G, Shen X, Lei H, Han B, Xia K, Zhou C (2015) Selective adsorption of Gd<Sup>3+</Sup> on a magnetically retrievable imprinted chitosan/carbon nanotube composite with high capacity. ACS Appl Mater Interfaces 7(38):21047–21055. https://doi.org/10.1021/acsami.5b07560

Li R, Zhu Q, Lu S (2023) Adsorption of phosphate in water by defective Uio-66/Ce2(Co3)3 composite: adsorption characteristics and mechanisms. Appl Surf Sci 640:158459. https://doi.org/10.1016/j.apsusc.2023.158459

Liang X, Zeng Q (2024) Copolymers-functionalized metal-organic framework composite for efficient adsorption of rare-earth elements. Microporous Mesoporous Mater 366:112960. https://doi.org/10.1016/j.micromeso.2023.112960

Liu WJ, Hong GY, Dai DD, Li LM, Dolg M (1997) The Beijing four-component density functional program package (Bdf) and its application to Euo, Eus, Ybo and Ybs. Theor Chem Acc 96(2):75–83. https://doi.org/10.1007/s002140050207

Liu WJ, Wang F, Li LM (2003) The Beijing density functional (Bdf) program package: methodologies and applications. J Theor Comput Chem 2(2):257–272. https://doi.org/10.1142/s0219633603000471

Migaszewski ZM, Galuszka A (2015) The characteristics, occurrence, and geochemical behavior of rare earth elements in the environment: a review. Crit Rev Environ Sci Technol 45(5):429–471. https://doi.org/10.1080/10643389.2013.866622

Okamura H, Hirayama N (2021) Recent progress in ionic liquid extraction for the separation of rare earth elements. Anal Sci 37(1):119–130. https://doi.org/10.2116/analsci.20SAR11

Prabhu SM, Imamura S, Sasaki K (2019) Mono- di-, and tricarboxylic acid facilitated lanthanum-based organic frameworks: insights into the structural stability and mechanistic approach for superior adsorption of arsenate from water. ACS Sustain Chem Eng 7(7):6917–6928. https://doi.org/10.1021/acssuschemeng.8b06489

Qu J, Li Z, Wang S, Lin Q, Zhang Z, Wu Z, Hu Q, Jiang Z, Tao Y, Zhang Y (2024a) Enhanced degradation of atrazine from soil with recyclable magnetic carbon-based bacterial pellets: performance and mechanism. Chem Eng J 490:151662. https://doi.org/10.1016/j.cej.2024.151662

Qu JH, Li YH, Bi FX, Liu XY, Dong ZH, Fan HL, Yin M, Fu LB, Cao WD, Zhang Y (2024b) Smooth Vetch (Vicia Villosa Var.) coupled with ball-milled composite mineral derived from shell powder and phosphate rock for remediation of cadmium-polluted farmland: insights into synergetic mechanisms. Acs Es&t Eng 4(8):2054–2067. https://doi.org/10.1021/acsestengg.4c00177

Rad M, Borhani S, Moradi M, Safarifard V (2021) Tuning the crystallinity of Zro2 nanostructures derived from thermolysis of Zr-based aspartic acid/succinic acid mofs for energy storage application. Physica E-Low-Dimens Syst Nanostruct 134:114921. https://doi.org/10.1016/j.physe.2021.114921

Salahshoori I, Namayandeh Jorabchi M, Mazaheri A, Mirnezami SMS, Afshar M, Golriz M, Nobre MAL (2024) Tackling antibiotic contaminations in wastewater with novel modified-Mof nanostructures: a study of molecular simulations and Dft calculations. Environ Res 252:118856. https://doi.org/10.1016/j.envres.2024.118856

Tang J, Chen Y, Zhao M, Wang S, Zhang L (2021) Phenylthiosemicarbazide-functionalized Uio-66-Nh2 as highly efficient adsorbent for the selective removal of lead from aqueous solutions. J Hazard Mater 413:125278. https://doi.org/10.1016/j.jhazmat.2021.125278

Tong J, Chen L, Cao J, Yang Z, Xiong W, Jia M, Xiang Y, Peng H (2022) Biochar supported magnetic Mil-53-Fe derivatives as an efficient catalyst for peroxydisulfate activation towards antibiotics degradation. Sep Purif Technol 294:121064. https://doi.org/10.1016/j.seppur.2022.121064

Wang C, Liu X, Chen JP, Li K (2015) Superior removal of arsenic from water with zirconium metal-organic framework Uio-66. Sci Rep 5:16613. https://doi.org/10.1038/srep16613

Wang Y, He L, Li Y, Jing L, Wang J, Li X (2020) Ag Nps supported on the magnetic Al-Mof/Pda as nanocatalyst for the removal of organic pollutants in water. J Alloys Compd 828:154340. https://doi.org/10.1016/j.jallcom.2020.154340

Wang Y-Y, Lu H-H, Liu Y-X, Yang S-M (2016) Ammonium citrate-modified biochar: an adsorbent for La(Iii) ions from aqueous solution. Colloids Surf A 509:550–563. https://doi.org/10.1016/j.colsurfa.2016.09.060

Xie Z, Diao S, Xu R, Wei G, Wen J, Hu G, Tang T, Jiang L, Li X, Li M, Huang H (2023) Construction of carboxylated-Go and Mofs composites for efficient removal of heavy metal ions. Appl Surface Sci 636:157827–157829. https://doi.org/10.1016/j.apsusc.2023.157827

Yan L, Song X, Miao J, Ma Y, Zhao T, Yin M (2024) Removal of tetracycline from water by adsorption with biochar: a review. J Water Proc Eng 60:105215. https://doi.org/10.1016/j.jwpe.2024.105215

Yang F, Zhao L, Gao B, Xu X, Cao X (2016) The interfacial behavior between biochar and soil minerals and its effect on biochar stability. Environ Sci Technol 50(5):2264–2271. https://doi.org/10.1021/acs.est.5b03656

Yongxing W, Xiaorong W, Zichun H (2000) Genotoxicity of Lanthanum (Iii) and Gadolinium (Iii) in human peripheral blood lymphocytes. Bull Environ Contam Toxicol 64(4):611–616. https://doi.org/10.1007/s001280000047

Zhang Y, Suo B, Wang Z, Zhang N, Li Z, Lei Y, Zou W, Gao J, Peng D, Pu Z, Xiao Y, Sun Q, Wang F, Ma Y, Wang X, Guo Y, Liu W (2020) Bdf: a relativistic electronic structure program package. J Chem Phys 152(6):064113. https://doi.org/10.1063/1.5143173

Zhang J, Chen Z, Liu Y, Wei W, Ni B-J (2024a) Removal of emerging contaminants (Ecs) from aqueous solutions by modified biochar: a review. Chem Eng J 479:147615. https://doi.org/10.1016/j.cej.2023.147615

Zhang G, Zhou L, Tan X, Fang Y, Du C, Bao X, Zeng Y, Ma W, Yan Z (2024b) Endogenous iron-enriched biochar loaded nickel-foam cathode in electro-fenton for ciprofloxacin degradation: performance, mechanism and Dft calculation. Chem Eng J 498:155446. https://doi.org/10.1016/j.cej.2024.155446

Zhao X, Jiang X, Peng D, Teng J, Yu J (2021) Behavior and mechanism of graphene oxide-tris(4-aminophenyl) amine composites in adsorption of rare earth elements. J Rare Earths 39(1):90–97. https://doi.org/10.1016/j.jre.2020.02.006

Zhou D, Chen X, Liang B, Fan X, Wei X, Liang J, Wang L (2019) Embedding Mil-100(Fe) with magnetically recyclable Fe3O4 nanoparticles for highly efficient esterification of diterpene resin acids and the associated kinetics. Microporous Mesoporous Mater 289:109615. https://doi.org/10.1016/j.micromeso.2019.109615